Proceedings of Global Power and Propulsion Society
ISSN-Nr: 2504-4400
GPPS Chania22
September 12th–14th, 2022

www.gpps.global

GPPS-TC-2022-0013

A NOVEL AND COST-EFFECTIVE APPROACH TO SIMULATING DYNAMIC STALL ON ROTATING WIND TURBINE BLADES WITH A CHANGING ANGLE OF ATTACK

Jan Dominik Ahrens **Mark Ziesse** **Lars Wein** **Joerg R. Seume**

ahrens@tfd.uni-hannover.de

Institute of Turbomachinery and Fluid Dynamics

Leibniz Universität Hannover

Hannover, Germany

ABSTRACT

The flow around wind turbine blades dynamically stalls when the local angle of attack temporarily rises above the angle of static separation. This introduces increased loads, which can lead to the destruction of the blade. The research reported here provides a computational fluid dynamics setup in OpenFOAM that solves the unsteady Reynolds-averaged Navier-Stokes equations to investigate dynamic stall on WT blades. The rotating and pitching motion of the blades is implemented via a novel combination of a dynamic and a sliding mesh approach. Simulations are carried out with different mesh resolutions and the results are compared with experimental data. It is shown that the usage of wall functions in the boundary layer is not suitable for investigating dynamic stall. When resolving the boundary layer instead, the results correctly predict the characteristics of a dynamic stall hysteresis with a maximum deviation of 8%. With the help of the developed setup, the computational effort of investigating dynamic stall on a large wind turbine (rated capacity 20 MW) can be reduced by 10% to approx. $\approx 2.8 \cdot 10^6$ CPUh when compared to similar setups in the literature.

INTRODUCTION

The power of a wind turbine (WT) increases quadratically with its rotor diameter, which drives the increase in size of future WTs. These WTs will reach rated capacities of approx. 20 MW. The long, slender, and flexible rotor blades of such megastructures will be more susceptible to deformations compared to today's rotor blades leading to dynamic changes in the local angle of attack (AoA). Besides the deformation of the blade, the AoA is affected by fluctuations in wind speed and turbulence and an altitude-dependent wind speed distribution, which becomes more important for increasing WT diameters. An AoA above the angle of static separation causes the flow at the profile to enter the range of dynamic stall, which leads to transient loads that excite aeroelastic interactions between the flow and the blade (Leishman, 2002). This additional excitation may lead to mechanical fatigue and in the case of resonance leads to the destruction of the rotor blade. The consideration of these loads and the associated aeroelastic stability of the rotor blade is therefore a decisive factor in the design of future WT structures (Veers et al., 2019; Adema et al., 2020).

Dynamic stall has been a subject of research in the field of helicopter aerodynamics for many years (Leishman, 2006; Corke and Thomas, 2015). The influence of dynamic stall on the blades has been researched by the means of experimental investigations as in Merz et al. (2017) and Schwermer et al. (2019) and of computational fluid dynamics (CFD) (Letzgus et al., 2019). A comparison between 2D and 3D simulations conducted in Kaufmann et al. (2017) has shown the importance of analyzing dynamic stall as a three-dimensional phenomenon, because of span-wise vortices travelling along the blade. According to Guntur and Sørensen (2015), the rotation of the blade leads to the delay of the initiation of the separation of the flow and therefore to increased loads. This is why the rotation of the rotor blade should be considered when analyzing dynamic stall. Due to the size of wind turbines, experimental data for dynamic stall events of full rotors (rotating) is only available for smaller WTs as in Butterfield et al. (1991) and Hand et al. (2001). To investigate dynamic stall on WT

megastructures, either experiments of scaled WTs as in Berger and Kühn (2018), or CFD simulations have to be conducted. In contrast to helicopter blades, the large rotors (Radius R = 180m) lead to high Reynolds numbers ($\mathrm{Re} \approx 2 \cdot 10^7$) and low Mach numbers ($\mathrm{Ma} < 0.3$). Together with the complex physics of a dynamic stall event, these high Reynolds numbers are associated with a high computational effort. Therefore, CFD simulations of large rotors have only been carried out for static AoAs (Bangga et al., 2017; Bangga, 2018) (rated capacity = 10 MW) and for small rotors when also simulating a changing AoA (Letzgus et al., 2019; Guntur et al., 2016). The combination of the rotating and pitching motion of the blade for the latter cases has been implemented via an overset mesh or a deformable mesh approach, respectively. State of the art reduced order models for predicting loads due to dynamic stall on WT blades rely on experimental data or CFD results from existing airfoil geometries and are thus semi-empirical (Adema et al., 2020; Rocchio et al., 2020; Mohamed and Wood, 2021). Larger rotor blades will lead to modified airfoil geometries (Zalkind et al., 2019) for which the reduced order models have not been tested. Further, to the best of the authors knowledge, none of these models have been validated for Reynolds numbers of $\approx 2 \cdot 10^7$.

In the present work, a CFD setup for the open-source flow solver OpenFOAM v2012 is developed for investigating dynamic stall on rotating rotor blades with a changing AoA. The setup is to be used for a parameter study that aims to find the correlation of basic airfoil design parameters of WT megastructures with dynamic stall. With the results of the parameter study a reduced order model for dynamic stall can be developed, which is valid for airfoil geometries of future WT megastructures at high Reynolds numbers. This is helpful for predicting the transient loads in the design process and for developing new airfoil geometries that are less susceptible to dynamic stall. Because of the immense computational resources of approx. $3.1 \cdot 10^6$ CPUh per simulation required for such a study (scaled computational effort of the simulations in Letzgus et al. (2019)), the secondary objective of this work is to develop a cost-effective setup by reducing the computational effort to a minimum. The setup is validated with the experimental data from Schwermer et al. (2019). A functional parameter study requires the setup to capture the following characteristics of the dynamic stall hysteresis: the dynamic load peak and the further increase of the lift coefficient when surpassing the angle of static separation. A novel combination of sliding and dynamic mesh approaches is implemented to capture the rotational and pitching motion of the blades. Symmetry conditions of the rotor are taken into account and the SST model (Menter, 1994) provides turbulence closure for solving the unsteady Reynolds-averaged Navier-Stokes (URANS) equations. In a second step, this standard SST model is extended with the $\gamma - \mathrm{Re}_\Theta$ transition model by Langtry and Menter (2009) and the results are compared with each other. A driving factor of the computational effort is the number of cells of the mesh. Therefore, the mesh resolution necessary for accurately calculating integral loads, such as the lift, is determined by comparing two meshes for simulations of a pitching blade section.

METHODOLOGY

Modelling Description

The overall objective of the underlying research project is to take into account the detachment processes in the design of WTs. This requires an accurate prediction of these detachment processes by means of CFD simulations. The most accurate simulation method currently applicable for technically relevant flows is the Large Eddy Simulation (LES), which is used by Schneider et al. (2011) to simulate turbulent separated flow with a Reynolds number of $\mathrm{Re} \approx 1 \cdot 10^4$. According to Zieße et al. (2020), approx. $20 \cdot 10^6$ cells are sufficient to reproduce a separation-induced transition on an airfoil by LES with a chord length of $c = 0.1$ m (height-to-chord ratio $h/c \approx 0.3$) and the velocity in the free stream $u_\infty = 98$ m/s. These dimensions are associated with a Reynolds number of $\mathrm{Re} \approx 2 \cdot 10^5$ related to the airfoil chord and a computational effort of $\approx 0.4 \cdot 10^6$ CPUh. However, the wind turbines to be investigated later are to be simulated at Reynolds numbers of $\mathrm{Re} \approx 2 \cdot 10^7$ (Schepers et al., 2018; Bangga et al., 2018). According to Pope (2000), the dimension of the smallest eddies of a flow is $\propto \mathrm{Re}^{-\frac{3}{4}}$. To maintain the same relative mesh resolution, the cell width in each spatial direction and the time step size would have to be reduced by a factor of $Re^{-\frac{3}{4}}$. Assuming ideal parallelization, this would increase the computational effort for $\mathrm{Re} \approx 2 \cdot 10^7$ by a factor of $\approx 1 \cdot 10^6$. Thus, according to the current status, no LES of a wind turbine is feasible with a realistic Reynolds number and sufficient mesh resolution. Nonetheless, hybrid methods also have too high demands on the computational resources for simulations of the full blade of the large WTs. Assuming linear scalability of the computational effort of the Detached-Eddy Simulations (DES) conducted in Letzgus et al. (2019), a fully resolved DES of a large WT requires $\approx 2.2 \cdot 10^{10}$ CPUh. Consequently, and with a view to the overall research objective, the subject of this work are URANS simulations of large WTs.

The discretization of the governing system of equations is based on a 2$^{\mathrm{nd}}$ order finite volume approach in space and time. The spatial discretization is a 2$^{\mathrm{nd}}$ order upwind method according to Warming and Beam (1976) and the temporal discretization corresponds to the implicit three-point backward Euler scheme. The additional terms resulting from the turbulence are modelled by means of the SST (Menter, 1994). For comparison, a simulation with the $\gamma - \mathrm{Re}_\Theta$ transition model by Langtry and Menter (2009) is conducted. The influence of the mesh movement is taken into account by correcting the predominant fluxes in the affected cells. This is done by replacing the velocity with a relative velocity in all convection

Table 1 Non-dimensional cell sizes of the coarse mesh of test case A. The values for the fine mesh are half the size.

Name: \ Value:	Δx^+_{max}	y^+_{max}	Δz^+_{max}
Leading edge	182	1.78	2808
Trailing edge	76	0.46	772
Pressure side	704	0.19	366
Suction side	582	0.31	596

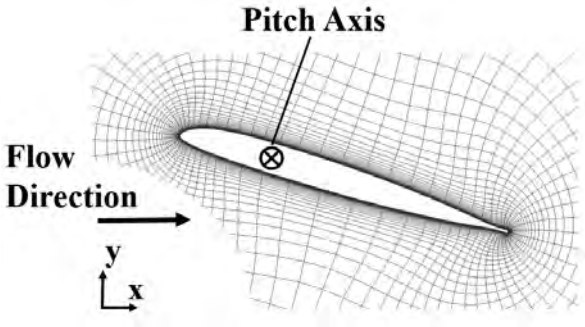

Figure 1 2D view of the computational domain of test case A

terms. A detailed description is provided in Jasak (2009). The resulting system of equations is solved using the *pimpleFOAM* solver of the open-source simulation software package OpenFOAM. The pressure-velocity coupling is based on the Pressure-Implicit Split Operator (PISO) in Issa (1986). The equations itself are solved with a preconditioned bi-conjugate gradient method.

Test Cases

In this work, two cases are defined to investigate flow separation around a rotor blade with the DSA-9A airfoil shape. The radius of the blade considered is $R = 0.65$ m and the chord length is $c = 0.072$ m with a height-to-chord ratio of $\frac{h}{c} = 0.14$. In test case A, a section of the blade at $r = 0.77R$ is used with a span-wise length of 0.02 m $= 0.03R$ to simulate dynamic stall while ignoring the rotational motion of the blade. Simulating this case with two different mesh resolutions serves to test the setup and verify the necessary mesh resolutions for resolving integral loads. The computational domain of this test case A is shown in Fig. 1.

A fixed velocity of $u = 74.1$ m/s is specified at the inlet using a Dirichlet boundary condition resulting in a Reynolds number of $\mathrm{Re} = 4.4 \times 10^5$. The inlet velocity corresponds to the resulting angular velocity at $r = 0.77R$ of the rotating blade. The flow is assumed incompressible and a constant static pressure is imposed at the outlet. A no-slip boundary condition is set on the blade itself and the boundary layers are assumed fully turbulent. A periodicity condition is applied at the span-wise edges of the blade section. All other boundary conditions correspond to a Neumann boundary condition with $\frac{\partial}{\partial n}\phi = 0$. Furthermore, a periodic pitching of the blade is imposed with a root pitch angle (RPA)

$$\Theta(t) = 23.8^\circ - 6.2^\circ sin(2\pi f_{\mathrm{rot}} t) \tag{1}$$

and $f_{\mathrm{rot}} = 23.6$Hz. The pitch axis lies at $c/4$ of the blade in the direction of axis Z. The angle of static separation is reached at an RPA of $\Theta_s = 26.5^\circ$ (Schwermer et al., 2019). The mesh resolution for the coarser mesh is given in Tab. 1. The non-dimensional cell sizes normal to the wall are determined with the phase averaged wall shear stresses τ_w, the density ρ, the kinematic viscosity ν and the distance between the cell center and the wall y. Non-dimensional cell sizes perpendicular to the wall are calculated accordingly but with the chord-wise and span-wise cell sizes Δx and Δz:

$$y^+ = \frac{y \cdot \sqrt{\tau_w/\rho}}{\nu} \tag{2}$$

$$\Delta x^+ = \frac{\Delta x \cdot \sqrt{\tau_w/\rho}}{\nu} \tag{3}$$

Because of the applied pitch motion, the wall shear stresses and therefore the non-dimensional cell sizes are unsteady. The presented values are the maximum values in the respective areas for all RPAs. The cells of the surrounding domain are created with a constant growth factor of 1.2. The finer mesh resolution is created by cutting every cell in half for every spatial direction, increasing the overall cell count by factor 8. Thereby, the increased mesh resolution does not change the geometrical discretization.

In test case B, the full rotor with a combined rotational and pitching motion is analyzed. Two meshes for the full rotor blade are created in Pointwise©:

1. A coarse mesh with Δx^+_{max} and Δz^+_{max} shown in Fig. 2 but with the initial cell center height: $30 < y^+ < 50$. The boundary layer is modelled utilizing wall functions. Total number of cells $= 5.5 \cdot 10^6$.
2. A finer mesh with cell sizes as shown in Tab. 2. The boundary layer is fully resolved. Total number of cells $= 10.8 \cdot 10^6$.

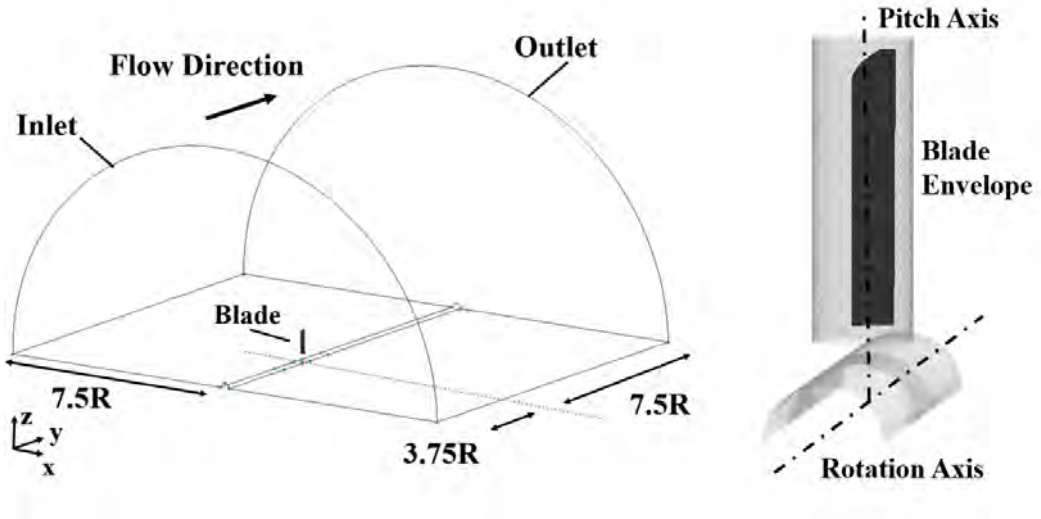

Figure 2 Computational domain of test case B (left) and detailed view of the blade and blade envelope (right)

Table 2 Cell sizes of the mesh resolving the boundary layer (test case B)

Name: \ Value:	Δx^+_{max}	y^+_{max}	Δz^+_{max}
Leading edge	148	4.5	2100
Trailing edge	60	1.2	580
Pressure side	370	0.9	354
Suction side	322	1.68	694

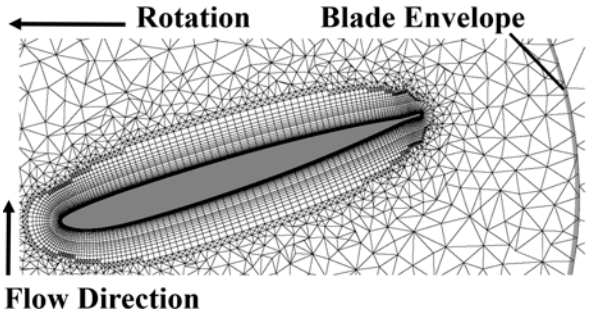

Figure 3 Top view of the blade envelope at r= 0.77R for test case B

A hyperbolic extrusion is applied to the structured surface mesh of the blade resulting in the boundary layer meshes consisting of quad cells. As in test case A, the cell sizes increase with a growth factor of 1.2 away from the wall. The same growth factor is used to create the cells in the surrounding domain. The blade hub is not considered in the mesh generation. In the direction of rotation, the periodicity of the geometry is used so that only one blade is simulated. While test case A has no rotational motion, test case B has two mesh movements. The complete computational domain is rotated along the rotation axis Y (see Fig. 2) with a constant speed of $\omega = 2\pi f_{rot}$. According to the experiment, the pitch frequency is chosen to be identical to the rotor frequency f_{rot}, so that one rotor revolution corresponds to one pitch period. To simulate this complex superimposed mesh motion, a sliding mesh approach (cyclicAMI) is used on the edge between the mesh of the blade envelope and the outer computational domain (see Fig. 3). The cells at the blade envelope and the outer computational domain are not connected so that they can slide off of each other when the blade pitches. The face values of these two interfaces are computed via linear interpolation between neighboring cell values. A fixed velocity of $u = 2.4149$ m/s is specified at the inlet and a constant static pressure is imposed at the outlet. The flow is assumed incompressible. These conditions correspond to the experimental studies from Schwermer et al. (2019), which are used to validate the setup with test case B. A detailed description of the experimental setup at the German Aerospace Center (DLR) in Goettingen is provided in Schwermer et al. (2016).

The maximum Courant-Friedrichs-Lewy number (CFL number) for which the simulations converge is CFL < 15 for test case A and for test case B CFL < 80. This results in an azimuthal time step for test case B of $\Delta\psi \approx 1/13°$, which corresponds to the pressure sensor sampling frequency of the experiment. To reduce the computational cost to a minimum, the maximum time steps are chosen for the simulations. The initial transient is determined by applying the approach in Ries et al. (2018) for scale-resolving simulations to the conducted URANS simulations. The instantaneous lift coefficient hysteresis are computed for the last 12 simulated revolutions (24 in total for test case B). With the help of an autocorrelation function, confidence intervals with a 95%-confidence level are determined for every time step. Stationarity (end of initial transient) is assumed when 95% of the lift coefficients for every time step fall within the estimated confidence intervals. The same procedure is applied for test case A by computing the confidence intervals with the last 11 pitch cycles. Thereby, in

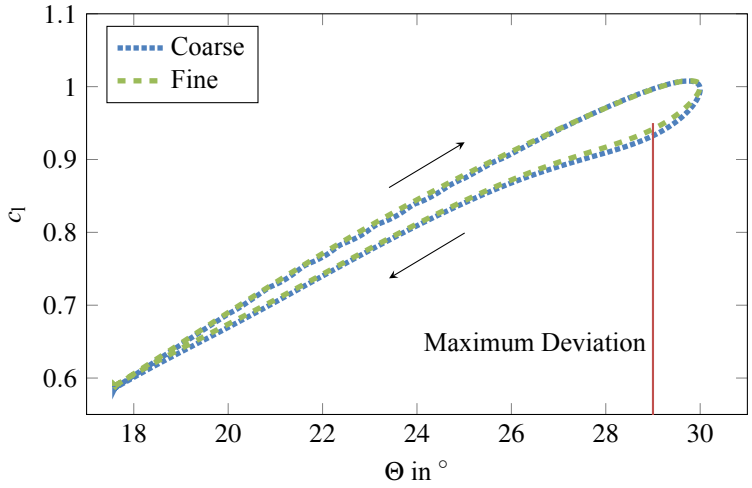

Figure 4 Phase averaged sectional lift coefficients for the coarse and fine mesh resolutions of test case A. The maximum sampling error for the phase averaged URANS values is $\pm 5.2 \cdot 10^{-5}$.

test case A 12 profile overflows are initially simulated for the transient of the flow, and 19 rotor revolutions for test case B. After the transient, 10 more profile overflows are simulated for test case A and 5 rotor revolutions for test case B to conduct phase averaged values of the flow. The statistical convergence of the phase averaged values is verified by determining sampling error intervals as in Ries et al. (2018). The intervals are visualized with error bars in the respective figures and 95% of the instantaneous values that are used for phase averaging fall within these intervals. The computational cost for test case B with the boundary layer resolving mesh resolution is $\approx 8 \cdot 10^4$ CPUh. Assuming linear scalability, a simulation of a large WT with a rated power of approx. 20 MW using this CFD setup requires $\approx 2.8 \cdot 10^6$ CPUh.

RESULTS

Test Case A

In test case A, a section of the blade at $0.77R$ is used to verify the necessary mesh resolution for resolving integral loads during a dynamic stall event. For the future research of large WTs, the parameters to be investigated are the lift and the drag, which depend on the pressure distribution on the airfoil. According to Clancy (1975), the sectional lift coefficient is calculated with the velocity u, the lift force per unit span l, and the chord length c:

$$c_l = \frac{l}{\rho u^2 c} \tag{4}$$

In Fig. 4, the sectional lift coefficients for the two mesh resolutions of test case A are visualized as a function of the RPA $\Theta(t)$. In both cases the minimum lift occurs at $\Theta(t)_{\text{min}} = 17.6°$. With an increasing RPA, the lift increases and a maximum is reached at $\approx 29.7°$. Inversely, the lift decreases when the RPA decreases. The characteristic lift hysteresis loop of a dynamic stall event as described in Butterfield et al. (1991) is captured for both mesh resolutions and the lift for a decreasing RPA is lower than for an increasing one. There is no dynamic load peak (lift overshoot) at $\Theta(t)_{\text{max}} = 30°$, which would be characteristic for a dynamic stall event. However, this is in accordance with the results from Guntur et al. (2016) and is due to the missing influence of the rotation of the blade. The maximum deviation between the two simulations occurs at $\Theta = 29°$ during the downstroke and amounts to 0.85%. These results indicate that $\Delta x^+ < 700$ and $\Delta z^+ < 2800$ are sufficient for investigating the lift hysteresis of a dynamic stall event. It should be noted that refining the mesh even further and thereby increasing the cell count by factor 8 could decrease the maximum deviation. However, a simulation of a large WT with such a mesh would require $\approx 70 \cdot 10^6$ CPUh which is unfeasible for a parameter study.

Test Case B

In test case B, the full rotor with a combined rotational and pitching motion is simulated and the results are validated with the experimental data from Schwermer et al. (2019). The phase averaged values are calculated with 4557 data points per rotor revolution. The resulting sectional lift coefficients of test case B are visualized in Fig. 5. The error bars for the experimental data from Schwermer et al. (2019) are visualized for every 440 data points.

The results of the simulation utilizing wall functions underpredict the minimum lift at $\Theta = 17.6°$ by $\approx 10.5\%$. Increasing the RPA leads to an increase of the lift until $\Theta \approx 27.8°$. The dynamic lift peak happens 2.4° earlier than in the experiment and is overpredicted by 2.7%. Exceeding this RPA, the lift decreases which is a non-physical behavior compared to the experiment. During the downstroke motion, the lift is underpredicted by up to 40%. The simulation with the standard SST

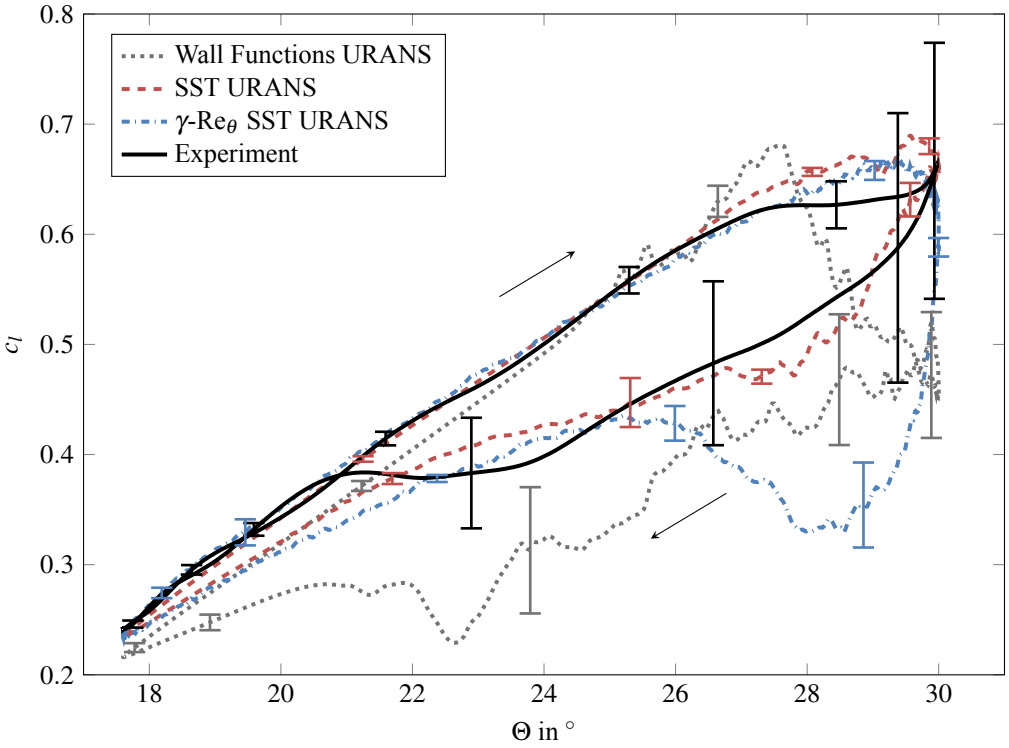

Figure 5 Phase averaged sectional lift coefficients of experiment (black) and URANS with wall functions (grey) and resolved boundary layer (BL) (red) and transition model ($\gamma - \mathrm{Re}_\theta$) (blue) for blade section r$= 0.77$R. The sampling errors for the phase averaged URANS values are visualized when $> 2.5 \cdot 10^{-3}$.

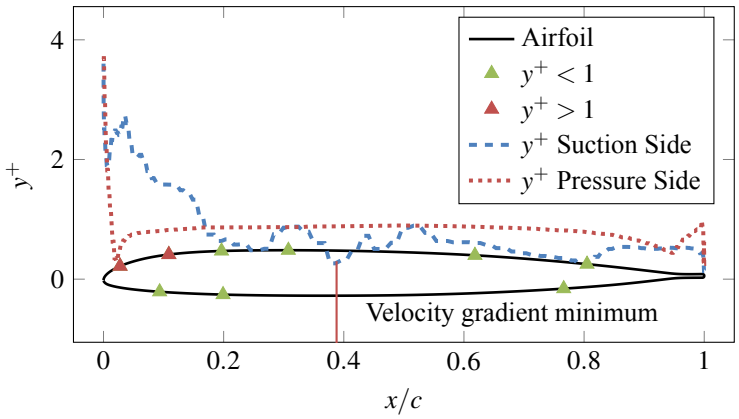

Figure 6 Non-dimensional cell size distribution y^+ at the wall (blue: suction side; red: pressure side) for $\Theta = 28.67°$ during upstroke for the standard SST turbulence model. The triangles are the pressure sensor positions from the experiment with the color corresponding to the respective cell sizes in the simulation (green: $y^+ < 1$; red: $y^+ > 1$).

model and resolved boundary layer predicts the lift within the experimental uncertainties during the upstroke motion of the blade for $18.6° < \Theta < 27°$. For $17.6° < \Theta < 18.6°$, the maximum deviation is 2.7%. When exceeding $\Theta = 27°$ the lift curve flattens as in the experiment and the dynamic lift peak at $\Theta_{max} = 30°$ is predicted within the experimental uncertainties. The maximum deviation during the upstroke motion of approx. 6.7% occurs for $\Theta = 28.67°$. In analogy to test case A, the lift is lower during the downstroke than during the upstroke motion. The lift during the downstroke is captured within the experimental uncertainties for $30° > \Theta > 21.4°$. Between $21.4° > \Theta > 17.6°$ the maximum deviation is 8.2%. As in the experiments, the sampling error increases for $\Theta > 27°$ during the upstroke and for $\Theta > 21°$ during the downstroke motion, which is due to the unsteadiness of a dynamic stall event. For the SST model extended with the γ-Re_θ transition model, the upstroke motion is captured within the experimental uncertainties for $23.5° < \Theta < 28.5°$. The maximum deviation between $17.6° < \Theta < 23.5°$ is 3.7%. The results show a similar flattening of the lift curve as the results from the standard SST model but the maximum deviation is reduced to 5.4% for $27° < \Theta < 30°$. The largest difference between the two

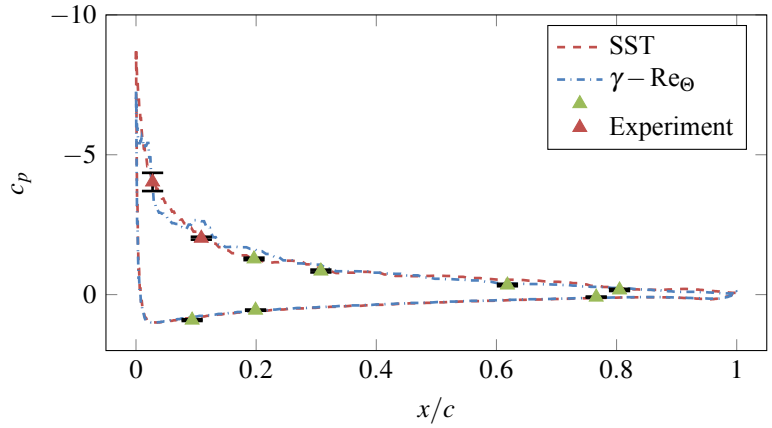

Figure 7 Phase averaged pressure distributions of URANS and experiment at $\Theta = 28.67°$ during upstroke. The triangles are the pressure values from the experiment with the color corresponding to the respective cell sizes at these positions in the simulation (green: $y^+ < 1$; red: $y^+ > 1$).

models occurs during the downstroke motion for $30° > \Theta > 26.5°$. While the standard SST model predicts this interval within the experimental uncertainties, the lift for the extended model drops strongly to a maximum deviation of 39.7%. For $26.5° > \Theta > 21.7°$, the lift is again predicted within the experimental uncertainties and between $21.7° > \Theta > 17.6°$ the maximum deviation is 11%.

A comparison between the two meshes shows that the results are highly dependent on the treatment of the boundary layer. It is evident that modelling the boundary layer with wall functions is not suitable for investigating dynamic stall because the flow detaches prematurely and the characteristic lift hysteresis is not captured. By contrast, the mesh resolving the boundary layer captures the distinct dynamic stall hysteresis for both turbulence models. The γ-Re_θ transition model improves the results during the upstroke motion when the AoA exceeds the angle of static separation. However, the downstroke motion and the reattachment of the flow is predicted more accurately by the standard SST model. An explanation for this behavior can be found in the mesh resolution of the boundary layer. For the mesh resolving the boundary layer, both Δx^+ and Δz^+ correspond to the cell sizes of the coarse mesh of test case A while y^+ exceeds the recommended limits. The cell sizes at the wall are therefore examined to analyze the deviations of the two turbulence models. The y^+ values of the standard SST model for the maximum deviation during the upstroke motion at $\Theta = 28.67°$ are visualized in Fig. 6. The graphs show that the highest y^+ values occur at the leading edge ($y^+ < 4$), which is in accordance with the high wall shear stresses to be expected in this region. The $y^+ < 1$ recommendation is not met for 2 pressure probes which are used to calculate the lift coefficients. It could be the case that the pressure values at these probes are causing the deviation from the experiment. To locally compare the experimental and URANS pressure distributions on the blade, the non-dimensional pressure coefficients are calculated as

$$c_\mathrm{p} = \frac{p - p_\infty}{0.5 \rho u^2} \tag{5}$$

with the pressure on the blade p and the pressure in the freestream p_∞. Surprisingly, Fig. 7 shows that for the standard SST model, the probe close to the leading edge ($x/c = 0.028$) predicts the pressure coefficient within the experimental uncertainties, despite $y^+ \approx 2.5$. The maximum deviation for probes with $y^+ > 1$ is 4.1%. This is consistent with the good results from test case A where $y^+ > 1$ at the leading edge of the coarse mesh. Instead, the highest deviations of up to 101.3% occur between $0.6 < x/c < 0.85$ on the suction side of the blade for two probes with $y^+ < 1$. In Fig. 6, it can be seen that y^+ reaches a minimum for $x/c = 0.39$, which is equivalent to the wall shear stress and therefore the velocity gradient reaching a minimum (see Eq. 2). This is an indication of a separation point of the flow and thus, the two pressure probes being located in an area of separated flow. Since the flow is assumed fully turbulent with the standard SST model, the transition of the boundary layer is not considered, which can lead to errors in predicting the lift (Michna et al., 2021) and the location of the separation point (Dong et al., 2019). Extending the SST model with the $\gamma - \mathrm{Re}_\Theta$ transition model improves the prediction of the pressure between $0.6 < x/c < 0.85$ to a maximum deviation of 35%. However, the transition model overpredicts the pressure at the leading edge ($x/c = 0.109$) by 30%. The pressure coefficients on the suction side of the blade are identical for both models. This leads to the conclusion that the $\gamma - \mathrm{Re}_\Theta$ model is able to improve the simulation results when $y^+ < 1$ while the standard SST model proves to be less sensitive to $y^+ > 1$.

CONCLUSIONS

A cost-effective CFD setup for simulating dynamic stall on rotating rotor blades with a time-variable angle of attack was developed. The novel combination of sliding and dynamic mesh approaches captures the superimposed rotational and pitching motion of the blade. The setup solves the URANS equations with the SST turbulence model by Menter (1994), which can be extended with the γ-Re_θ transition model by Langtry and Menter (2009).

The computational effort of simulating a large WT (rated capacity 20 MW) was estimated to be approx. $\approx 3.1 \cdot 10^6$ CPUh. With the help of this setup the computational effort was reduced by 10% to approx. $\approx 2.8 \cdot 10^6$ CPUh.

Accurate prediction of integral loads during a dynamic stall event limits cell sizes perpendicular to the wall to $\Delta x^+_{\mathrm{max}} < 700$ and $\Delta z^+_{\mathrm{max}} < 2800$. A comparison with the experimental data from Schwermer et al. (2019) showed that the results are dependent on the treatment of the boundary layer. Wall functions have proven to be unsuitable, as the lift decreases in a non-physical way after exceeding the angle of static separation. The maximum deviation between the lift coefficients of the experiment and the simulation is 40% and occurs during the downstroke motion of the blade. By contrast, when resolving the boundary layer instead of using wall functions, the simulation captures the distinct dynamic stall hysteresis for both turbulence models. During the upstroke until the angle of static separation, the maximum deviation for the standard SST model is 2.5% and 3.7% for the SST γ-Re_θ model. When exceeding this angle, a further increase in lift can be observed which is characteristic for a dynamic stall event. For angles of attack higher than the angle of static separation during the upstroke motion, the γ-Re_θ model improves the results by reducing the maximum deviation from 6.7% to 5.4%. The dynamic load peak is predicted within the experimental uncertainties for both models. The reattachment of the flow is captured within the experimental uncertainties for the standard SST model while being underpredicted by up to 39.7% by the γ-Re_θ model. An analysis of the local pressure coefficient distribution showed that the γ-Re_θ model can reduce the deviation from 101.3% to 35% in areas of separated flow when the non-dimensional cell sizes at the wall meet $y^+ < 1$. However, in areas of the blade where $y^+ > 1$, the deviation is increased from 4.1% to 30%. It can be said that the standard SST model is less sensitive to local coarse mesh resolutions while the γ-Re_θ model depends upon $y^+ < 1$ for the whole airfoil. Therefore, the results could be improved by refining the mesh in the vicinity of the leading edge for the γ-Re_θ model, which would increase the computational effort.

NOMENCLATURE

List Of Symbols

Symbol	Unit	Name
c	m	Chord length
c_l	-	Sectional lift coefficient
c_p	-	pressure coefficient
h	m	Blade heigt
f	s^{-1}	Rotational frequency
l	m	Blade span
p	$\frac{\mathrm{N}}{\mathrm{m}^2}$	Pressure
r	m	Radius
R	m	Radius of investigated blade
Re	-	Reynolds number related to airfoil chord
t	s	Time
u	$\frac{\mathrm{m}}{\mathrm{s}}$	Resulting velocity
x, y, z	m	Spatial coordinates
x^+, y^+, z^+	m	Non-dimensional spatial coordinates
Θ	$\circ$	Root pitch angle
ν	$\frac{\mathrm{m}^2}{\mathrm{s}}$	Kinematic viscosity
ρ	$\frac{\mathrm{kg}}{\mathrm{m}^3}$	Density
τ_w	$\frac{\mathrm{N}}{\mathrm{m}^2}$	Wall shear stress
Φ	-	Transported Quantity
ψ	$1/\circ$	Azimuthal time step
ω	$\mathrm{rad}\cdot\mathrm{s}^{-1}$	Angular velocity

Subscripts

max	Maximum
min	Minimum
rot	Rotor
s	static separation
∞	Infinity

Operators

Δ	Delta- / Difference
∂	Partial

Abbreviations

AoA	Angle of attack
CFD	Computational Fluid Dynamics
CFL	Courant-Friedrichs-Lewy
DES	Detached-Eddy Simulation
LES	Large-Eddy Simulation
RPA	Root pitch angle
URANS	Unsteady Reynolds-Averaged Navier-Stokes
WT	Wind turbine

ACKNOWLEDGMENTS

The authors thank the North-German Supercomputing Alliance (HLRN) and the cluster system at the Leibniz Universität of Hannover for the HPC resources, which have contributed to the development of the research results presented here. The present work has been carried out in the subprojects A02 within the Collaborative Research Center (CRC) 1463 "Integrated design and operation methodology for offshore megastructures" which is funded by the Deutsche Forschungsgemeinschaft (DFG, German Research Foundation). The authors thank the DFG for the support.
Further, the authors thank the German Aerospace Center in Göttingen (DLR) for providing the experimental data for the pitching rotor blade.

REFERENCES

Adema, N., Kloosterman, M. and Schepers, G. (2020), 'Development of a second-order dynamic stall model', *Wind Energy Science* **5**(2), 577–590.

Bangga, G. (2018), 'Comparison of blade element method and cfd simulations of a 10 mw wind turbine', *Fluids* **3**(4), 73.

Bangga, G., Weihing, P., Lutz, T. and Krämer, E. (2017), 'Effect of computational grid on accurate prediction of a wind turbine rotor using delayed detached-eddy simulations', *Journal of Mechanical Science and Technology* **31**(5), 2359–2364.

Bangga, G., Weihing, P., Lutz, T. and Krämer, E. (2018), Hybrid rans/les simulations of the three-dimensional flow at root region of a 10 mw wind turbine rotor, *in* 'New Results in Numerical and Experimental Fluid Mechanics XI', Springer, pp. 707–716.

Berger, F. and Kühn, M. (2018), Experimental investigation of dynamic inflow effects with a scaled wind turbine in a controlled wind tunnel environment, *in* 'Journal of Physics: Conference Series', Vol. 1037, IOP Publishing, p. 052017.

Butterfield, C., Simms, D., Scott, G. and Hansen, A. (1991), Dynamic stall on wind turbine blades, Technical report, National Renewable Energy Lab., Golden, CO (United States).

Clancy, L. J. (1975), *Aerodynamics*, John Wiley & Sons.

Corke, T. C. and Thomas, F. O. (2015), 'Dynamic stall in pitching airfoils: aerodynamic damping and compressibility effects', *Annual Review of Fluid Mechanics* **47**, 479–505.

Dong, H., Xia, T., Chen, L., Liu, S., Cui, Y., Khoo, B. and Zhao, A. (2019), 'Study on flow separation and transition of the airfoil in low reynolds number', *Physics of Fluids* **31**(10), 103601.

Guntur, S. and Sørensen, N. N. (2015), 'A study on rotational augmentation using cfd analysis of flow in the inboard region of the mexico rotor blades', *Wind Energy* **18**(4), 745–756.

Guntur, S., Sørensen, N. N., Schreck, S. and Bergami, L. (2016), 'Modeling dynamic stall on wind turbine blades under rotationally augmented flow fields', *Wind Energy* **19**(3), 383–397.

Hand, M. M., Simms, D., Fingersh, L., Jager, D., Cotrell, J., Schreck, S. and Larwood, S. (2001), Unsteady aerodynamics experiment phase vi: wind tunnel test configurations and available data campaigns, Technical report, National Renewable Energy Lab., Golden, CO.(US).

Issa, R. (1986), 'Solution of the implicitly discretised fluid flow equations by operator-splitting', *Journal of Computational Physics* **62**(1), 40–65.
URL: *https://doi.org/10.1016/0021-9991(86)90099-9*

Jasak, H. (2009), 'Dynamic mesh handling in OpenFOAM', *American Institute of Aeronautics and Astronautics* .
URL: *https://doi.org/10.2514/6.2009-341*

Kaufmann, K., Merz, C. B. and Gardner, A. D. (2017), 'Dynamic stall simulations on a pitching finite wing', *Journal of Aircraft* **54**(4), 1303–1316.

Langtry, R. B. and Menter, F. R. (2009), 'Correlation-based transition modeling for unstructured parallelized computational fluid dynamics codes', *AIAA journal* **47**(12), 2894–2906.

Leishman, G. J. (2006), *Principles of helicopter aerodynamics*, Cambridge university press.

Leishman, J. G. (2002), 'Challenges in modelling the unsteady aerodynamics of wind turbines', *Wind Energy: An International Journal for Progress and Applications in Wind Power Conversion Technology* **5**(2-3), 85–132.

Letzgus, J., Gardner, A. D., Schwermer, T., Keßler, M. and Krämer, E. (2019), 'Numerical investigations of dynamic stall on a rotor with cyclic pitch control', *Journal of the American Helicopter Society* **64**(1), 1–14.

Menter, F. R. (1994), 'Two-equation eddy-viscosity turbulence models for engineering applications', *AIAA Journal* **32**(8), 1598–1605.
URL: *https://doi.org/10.2514/3.12149*

Merz, C. B., Wolf, C., Richter, K., Kaufmann, K., Mielke, A. and Raffel, M. (2017), 'Spanwise differences in static and dynamic stall on a pitching rotor blade tip model', *Journal of the American Helicopter Society* **62**(1), 1–11.

Michna, J., Rogowski, K., Bangga, G. and Hansen, M. O. (2021), 'Accuracy of the gamma re-theta transition model for simulating the du-91-w2-250 airfoil at high reynolds numbers', *Energies* **14**(24), 8224.

Mohamed, A. and Wood, D. H. (2021), 'Modeling dynamic loads on oscillating airfoils with emphasis on dynamic stall vortices', *Wind Energy* **24**(11), 1225–1248.

Pope, S. B. (2000), *Turbulent Flows* -, Cambridge University Press, Cambridge.

Ries, F., Nishad, K., Dressler, L., Janicka, J. and Sadiki, A. (2018), 'Evaluating large eddy simulation results based on error analysis', *Theoretical and Computational Fluid Dynamics* **32**(6), 733–752.

Rocchio, B., Chicchiero, C., Salvetti, M. V. and Zanforlin, S. (2020), 'A simple model for deep dynamic stall conditions', *Wind Energy* **23**(4), 915–938.

Schepers, J., Boorsma, K., Sørensen, N., Sieros, G., Rahimi, H., Heisselmann, H., Jost, E., Lutz, T., Maeder, T., Gonzalez, A. et al. (2018), Final results from the eu project avatar: Aerodynamic modelling of 10 mw wind turbines, *in* 'Journal of Physics: Conference Series', Vol. 1037, IOP Publishing, p. 022013.

Schneider, H., Von Terzi, D. A., Bauer, H.-J. and Rodi, W. (2011), 'A mechanism for control of turbulent separated flow in rectangular diffusers', *Journal of fluid mechanics* **687**, 584–594.

Schwermer, T., Gardner, A. D. and Raffel, M. (2019), 'A novel experiment to understand the dynamic stall phenomenon in rotor axial flight', *Journal of the American Helicopter Society* **64**(1), 1–11.

Schwermer, T., Richter, K. and Raffel, M. (2016), Development of a rotor test facility for the investigation of dynamic stall, *in* 'New results in numerical and experimental fluid mechanics X', Springer, pp. 663–673.

Veers, P., Dykes, K., Lantz, E., Barth, S., Bottasso, C. L., Carlson, O., Clifton, A., Green, J., Green, P., Holttinen, H. et al. (2019), 'Grand challenges in the science of wind energy', *Science* **366**(6464).

Warming, R. F. and Beam, R. M. (1976), 'Upwind second-order difference schemes and applications in aerodynamic flows', *AIAA Journal* **14**(9), 1241–1249.
URL: *https://doi.org/10.2514/3.61457*

Zalkind, D. S., Ananda, G. K., Chetan, M., Martin, D. P., Bay, C. J., Johnson, K. E., Loth, E., Griffith, D. T., Selig, M. S. and Pao, L. Y. (2019), 'System-level design studies for large rotors', *Wind Energy Science* **4**(4), 595–618.

Zieße, M., , Wein, L., Müller-Schindewolffs, C., Herbst, F. and Seume, J. (2020), 'Validation of a synthetic-eddy method for modelling incoming wakes in scale-resolving simulations of turbomachinery cascades'.
URL: *https://doi.org/10.33737/gpps20-tc-17*